Impact of Transient Gas Injection on Flow-Induced Noise in Centrifugal Pumps

S. Wang, S. Yang, C. L. Shao[†] and J. F. Zhou

College of Mechanical and Power Engineering, Nanjing Tech University, Nanjing 211816, China

[†] *Corresponding author E-mail: chunlei-shao@njtech.edu.cn*

ABSTRACT

The influence of inlet gas volume fractions on flow-induced noise in centrifugal pumps during the transition process of gas injection and the generation mechanism of noise in this process was studied. To this end, numerical simulations of the flow and sound fields as well as visual experiments of the flow field were conducted. The variation laws of the flow field, frequency-domain sound field, and time-domain sound field during the process were investigated. The relationship between the pressure pulsation and flow-induced noise was analysed in detail. The results indicate that it is more reasonable to consider the outlet gas volume fraction as the judgement criterion for the end of the transition process. The axial and blade passing frequencies are characteristic discrete frequencies in this process. The pressure pulsation and sound pressure level at the blade passing frequency are stable in the early stage of the process. Subsequently, they decrease first and then increase in the middle stage and return to a stable state in the final stage. The variation laws of the two exhibit consistency, indicating that the pressure pulsation directly induces a change in the sound pressure level. Furthermore, the injection of gas can weaken the disturbance effect of the blade.

NOMENCLATURE

b	pump body thickness	Q_d	rated flow
c	propagation velocity of sound in the fluid	t	gas injection time
D_{in}	pump inlet diameter	Z	blade number
D_{out}	pump outlet diameter	φ_0	tongue placement angle
f_{max}	maximum calculation frequency	β_{1y}	blade inlet setting angle
F_S	sampling frequency	β_{2y}	blade outlet setting angle
F_N	sampling accuracy	η	efficiency
h	pump body height	ρ_{mix}	density of the mixture
H	head	ρ_l	liquid density
L	minimum grid size	ρ_g	gas density
N	number of samples	ω	angular frequency
n	rotational speed	λ	wavelength
P_{ref}	reference sound pressure		

1. INTRODUCTION

Centrifugal pumps are widely used in several industrial applications as energy conversion machinery and fluid transmission equipment. In this study, the process of stably transporting a single-phase medium to a gas–liquid two-phase medium in a centrifugal pump is called the transition process of gas injection. In this process, the transported medium is mixed with small bubbles and driven by high-speed rotation of the blade. Thus, the internal flow becomes extremely complex and is often accompanied by a high noise level, which affects the operational stability of the centrifugal pump. To ensure the safe operation of centrifugal pumps and solve the noise problem caused by gas–liquid two-phase flow, it is necessary to investigate the noise in pumps during the transition process of gas injection.

Centrifugal pump noise is typically classified as

mechanical or flow-induced noise. The mechanical noise problem has been addressed with continuous improvements in equipment manufacturing and assembly accuracy. The flow-induced noise problem has not been thoroughly studied because of its complex mechanism. The Lighthill acoustic simulation method initiated by Lighthill (1953, 1954) and continuously improved by Curle (1955), Goldstein (1973), Crighton (1972), and other researchers is widely used to solve all types of flow-induced noise problems. Lighthill's method combines computational fluid dynamics and computational acoustics to solve various flow-induced noise problems. Many scholars have conducted studies based on this method.

Regarding research on flow-induced noise inside the pump, Kalyan *et al.* (2013) and Rehman *et al.* (2013, 2015b, 2017) studied the flow characteristics of different centrifugal pumps. Rehman *et al.* (2015a) investigated the complex flow behaviour of a centrifugal pump under five different flow rates. Shao *et al.* (2021a, 2021b) used a high-speed camera to conduct visual experiments and study the flow law inside a pump under various operating conditions. Subsequently, research on the noise induced by gas–liquid two-phase flow in the pump was conducted, and the noise mechanism caused by the gas–liquid two-phase flow in the pump was preliminarily elaborated. Wang *et al.* (2017), Si *et al.* (2020), Liu *et al.* (2016), Gao *et al.* (2017), and Dong *et al.* (2018) studied the noise in centrifugal pumps under different operating conditions by performing experiments and numerical simulations. They analysed the effects of rotational speed, flow rate, cavitation (Rehman *et al.* 2013; Jaiswal *et al.* 2019, 2022), and backflow (Si *et al.* 2013) on flow-induced noise in pumps. Wang *et al.* (2019) evaluated the influence of different turbulence models on the accuracy of acoustic simulations. Their study serves as a reference for the reasonable selection of turbulence models. The mechanism of flow-induced noise in pumps has been well explained in previous studies.

The influence of solid structures on flow-induced noise has also been studied, and structural optimisation schemes for the noise reduction in centrifugal pumps have been proposed. Considering the influence of the solid wall and the natural frequency of pumps, He and Shao (2021), Jiang *et al.* (2007), and Rui and Zhao (2016) conducted investigated the radiation noise of centrifugal pumps using the acoustic-vibration coupling method. Based on existing research, some scholars have proposed structural optimisation schemes to reduce noise by adjusting the structural parameters of centrifugal pumps, such as the number of blades (Wang and Ding 2020), blade outlet angle (Guo *et al.* 2019), type of blade (Mousmoulis *et al.* 2019), and impeller outlet diameter (Luan *et al.* 2016). Most of the existing studies focused on centrifugal pumps under steady operating conditions and did not consider

flow-induced noise in pumps during the transition process of gas injection. Furthermore, they were all focused on the frequency-domain sound field and did not consider the time-domain sound field.

In this study, based on the acoustic analogy method, the flow and sound fields in a pump during the transition process of gas injection were numerically investigated using ANSYS Fluent 16.0 and LMS Virtual.Lab 13.6 software. The study was conducted as follows: 1) The flow in the pump was numerically simulated, and experiments on the external characteristics and internal flow were performed to verify the feasibility of the numerical simulation. 2) By monitoring the pressure and gas volume fraction (GVF) at the volute and outlet, a criterion for judging the end of the transition process of gas injection was established, and the flow law in the transition process of gas injection was analysed. 3) The frequency-domain acoustic field was numerically simulated during the transition process of gas injection, and the distribution of the sound pressure level (SPL) at the axial passing frequency (APF) and blade passing frequency (BPF) as well as the influence of the inlet GVF (IGVF) on the SPL were investigated. 4) The relationship between the pressure pulsation and SPL was established by
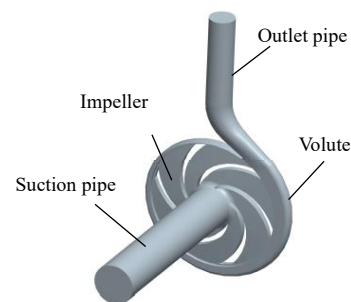

Fig. 1. Three-dimensional model of the fluid domain of the pump.

simulating the time-domain sound field during the transition process of gas injection, and the change law of the SPL with time at the BPF was analysed. The research results can serve as a valuable reference for the stable operation and design of high-efficiency and low-noise centrifugal pumps. In addition, the findings can be used for the time-domain numerical simulation of flow-induced noise.

2.   NUMERICAL SIMULATION METHOD

2.1 Numerical Simulation Method for the Flow Field

2.1.1 Three-dimensional Geometric Model

The research object in this study is the IS 80-50-250 centrifugal pump. A three-dimensional model of the fluid domain of the pump was built using Pro/Engineer 5.0. The fluid domain consisted of four

parts: suction pipe, impeller, volute, and outlet pipe. The lengths of the suction and outlet pipes were extended to avoid backflow at the inlet and outlet of the pump and ensure that the flow in the pump was fully developed. The three-dimensional model of the fluid domain is shown in Fig. 1, and the main parameters of the pump are listed in Table 1.

Table 1 Main parameters of the pump

Parameter	Dimension
Pump inlet diameter, D_{in} (mm)	80
Pump outlet diameter, D_{out} (mm)	50
Impeller outlet diameter, D_2 (mm)	250
Blade number, Z	6
Rotational speed, n (rpm)	2900
Rated flow, Q_d (m^3·h^{-1})	50
Base circle diameter, D_3 (mm)	260
Volute inlet width, b_3 (mm)	22
Tongue placement angle, φ_0 (°)	20
Blade outlet width, b_2 (mm)	9
Blade inlet angle, β_{1y} (°)	38
Blade outlet angle, β_{2y} (°)	32

2.1.2 Mesh and Monitoring Points

The grids of the centrifugal pump were meshed using ANSYS ICEM 16.0, as illustrated in Fig. 2. The suction and outlet pipes of the pump were divided into hexahedral structured grids. Owing to the complex structure of the impeller and volute, they were divided into tetrahedral unstructured grids. To improve the simulation accuracy, the grids near the volute tongue and blades were locally refined, and the grid independence was verified, as depicted in Fig. 3. When the grid number increases from $N4$ to $N5$, the head of the pump only increases by 0.3%, and the difference compared with the rated head of the pump (80 m) is only 3.2%, indicating that grid number $N4$ has met the simulation accuracy. The minimum grid is 0.5 mm, and the total number of grids is 1403215. The minimum orthogonal quality of the mesh is 0.3, the skewness of the mesh is approximately 0.35, and the minimum aspect ratio is 0.3. To save calculation time, this grid scheme was adopted for the numerical simulations. During the grid independence test, r=1.14, p=17.57, $GCI_{1,2}$ = 0.12%, and $GCI_{2,3}$ = 1.12%, so $GCI_{2,3} / (r^p \times GCI_{1,2})$ ≈ 1. Therefore, the grid independence can be ensured. To better study the variation law of the flow field in the pump during the transition process of gas injection (such as pressure and GVF), specific monitoring points were set on the middle section of the pump. The positions of each section and the monitoring points are displayed in Fig. 4, and the coordinates of the monitoring points are presented in Table 2.

2.1.3 Boundary Conditions and Simulation Route

Because the Fluent software has more physical models and better solution accuracy, it was applied to simulate the flow field in the pump during the transition process of gas injection. The Eulerian
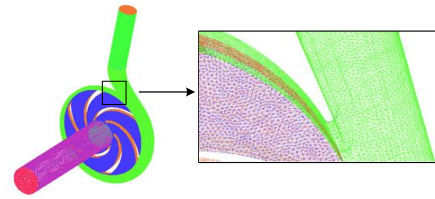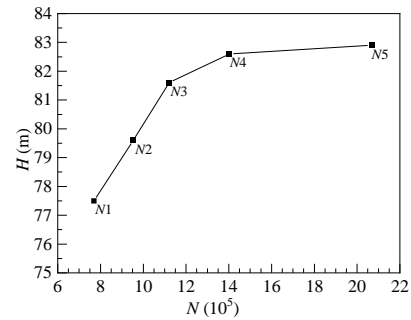

Fig. 2. Grids of the centrifugal pump.
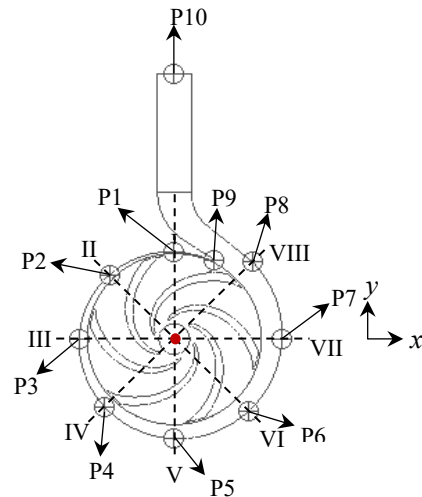

Fig. 3. Grid independence verification.

Fig. 4. Positions of sections and monitoring points.

Table 2 Coordinates of monitoring points.

Monitoring points	Coordinate (x, y, z) (mm)
P1	(0, 132.49, 0)
P2	(-96.94, 96.94, 0)
P3	(-141.79, 0, 0)
P4	(-103.44, -103.44, 0)
P5	(0, -151.17, 0)
P6	(110.16, -110.16, 0)
P7	(160.55, 0, 0)
P8	(116.89, 116.89, 0)
P9	(58.13, 120, 0)
P10	(0, 403, 0)

multiphase model was used to consider the two-phase flow, and the SST k–ω model was utilised as the turbulence model. Water was considered as a continuous phase, bubbles as a discrete phase, and the surface tension between the two phases was taken as 0.0717 N/m. The boundary conditions at the

pump inlet and outlet were the inlet and outflow velocities, respectively. The impeller rotation was set as the motion mesh.

To improve the calculation accuracy and convergence, first, the single-phase steady flow was simulated under the rated operating conditions (n_d = 2900 rpm, Q_d = 50 m^3/h, and Q_l = 0). Subsequently, the single-phase unsteady flow was solved based on the single-phase steady convergence. The time step was set to 0.00005747 s, that is, 1° of blade rotation, and the pressure at the outlet was monitored. The grid convergence factor was set to 10^{-4} to ensure grid independence. When the pressure at the outlet monitoring point reached a quasi-steady state with periodic oscillations and the mean value of the pressure tended to be stable, the calculation was considered to have converged. At that time, the pump was in a state of periodic unstable delivery of a single-phase liquid. Finally, based on unsteady simulation, the unsteady gas–liquid two-phase flow in the pump during the transition process of gas injection was solved by adjusting the gas flow rate to a certain value. At the same time, the pressure and the GVF at the outlet were monitored. When the pressure at the outlet reached a quasi-steady state with periodic oscillations and the mean value of the pressure and GVF tended to be stable, the transition process of gas injection was considered complete. At that time, the centrifugal pump was in a state of stably transporting a gas–liquid two-phase medium.

2.2 Numerical Simulation Method for the Sound Field

2.2.1 Acoustic Grid Inspection

The internal excitation source of the flow-induced noise in the pump can be divided into rotating and static dipole sound sources (Langthjem and Olhoff 2004). The rotating dipole sound source is the initial sound source produced by the high-speed rotation of the impeller. The static dipole sound source is generated by the continuous impact of the medium inside the impeller on the volute wall and jet-wake flow at the impeller outlet. The pressure pulsation on the volute wall produces noise, which is further intensified by the continuous refraction of the internal wall. In this study, a static dipole sound source was selected as the internal excitation source to study the variation law of the sound field in the pump during the transition process of gas injection.

Currently, the widely used mixed acoustic numerical simulation method is divided into two steps: (1) Set the medium as an incompressible fluid, simulate the unsteady flow field, and export the acoustic file. (2) Considering the compressibility of the fluid, the exported acoustic file is converted into a sound source with the same action form as the Lighthill method, and the acoustic solution is carried out. This method was used to simulate the sound field in the pump during the gas injection transition process. First, the unsteady flow in the transition process of

gas injection under different IGVFs was simulated, acoustic files in cgns format were obtained under various operating conditions, and the surface of the centrifugal pump was meshed for use as an acoustic grid in the LMS Virtual.Lab 13.6 software. Then, the solution type was set as the direct internal boundary element method in the acoustic boundary element module of the LMS Virtual.Lab 13.6 software. After the acoustic grid was imported, it was checked whether the upper limit frequency of the grid calculation satisfied the requirements and whether the grid directions pointed to the interior of the calculation domain. In acoustic calculations, the acoustic grid must satisfy Eq. (1).

$$L \le \frac{c}{6 f_{max}} \tag{1}$$

where L is the minimum grid size, c is the propagation velocity of sound in the fluid (m/s), and f_{max} is the highest frequency required for the calculation (Hz).

The calculation frequency of the acoustic grid was determined using the LMS Virtual.Lab 13.6 software. The calculation upper limit of the acoustic grid was 23144.9 Hz, whereas that of the flow field time step was 8700 Hz. The calculation upper limit frequency was much higher than the required frequency, which satisfied the calculation and analysis requirements. The directivity of the acoustic grid near the volute tongue was checked, as shown in Fig. 5. The arrows of the acoustic grid point to the interior of the computational domain, and the directivity of the grid satisfies the requirements. The size of the acoustic grid is 8 mm, which also meets the requirements described in Eq. (1).
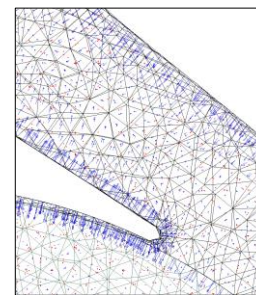

Fig. 5. Directivity check of the acoustic grid.

2.2.2 Physical Properties of the Medium

During the transition process of gas injection, the density of the medium in the pump changes with time. It can be considered that its density gradually changes from that of single-phase water to that of the final stable gas–liquid two-phase mixture. The evaluation of the medium density in the pump during the transition process of gas injection is discussed in this section.

The transition process of gas injection can be divided into three stages: first stage $t \leq t_1$, second stage $t_1 < t < t_2$, and third stage $t \geq t_2$, where t is the gas injection time. At $t = t_1$, the gas reaches the pump outlet. At $t = t_2$, the gas–liquid two-phase flow in the pump becomes stable, and the gas injection transition process is completed.

When $t \leq t_1$, the density of the mixture in the pump can be calculated using Eq. (2).

$$\rho_{\mathrm{mix}} = (1 - \mathrm{IGVF}\frac{t}{t_1})\rho_l + \mathrm{IGVF}\frac{t}{t_1}\rho_g \qquad (2)$$

where ρ_{mix} is the density of the mixture (kg/m³), ρ_l is the liquid density (kg/m³), and ρ_g is the gas density (kg/m³).

When $t_1 < t < t_2$, the density of the mixture in the pump can be calculated using Eq. (3).

$$\rho_{\mathrm{mix}} = \left(at^3 + bt^2 + ct + d \right)(\rho_g - \rho_l) + \rho_l \qquad (3)$$

where a, b, c, and d are obtained by fitting the GVF in the pump with time.

When $t \geq t_2$, the density of the mixture in the pump can be calculated using Eq. (4):

$$\rho_{\mathrm{mix}} = (1 - \mathrm{IGVF})\rho_l + \mathrm{IGVF}\,\rho_g \qquad (4)$$

When simulating the frequency-domain sound field in the pump during the transition process of gas injection, the density of the medium under the different operating conditions of IGVF = 1%, 2%, 3%, and 4% was set as the average density of the entire process. When simulating the time-domain sound field in the pump during the transition process of gas injection, the transition process was divided into several different sections by taking the impeller rotation of 360° as one cycle. The fluid density was set equal to the average density in each section, and the sound velocity was set to 1500 m/s. The fluid properties were assigned to the acoustic boundary mesh. Time-varying pressure pulsation files were imported and transformed into frequency-domain files through a Fourier transform, and the data were then transferred into an acoustic excitation file with the same effect as the pressure pulsation.

2.2.3 Boundary Conditions for the Sound Field Simulation

In the setting of the boundary conditions for the sound field numerical simulation, the converted pressure was used to define the acceleration boundary condition. The volute wall was set as the acceleration boundary. The sound absorption properties of the pump inlet and outlet were set to 1.5×10^6 Pa·s/m³. Acoustic field points comprising eight sections of the volute, volute tongue P9 (58.13, 120, 0), inlet point P0 (0, 0, 67.5), and outlet point P11 (0, 293, 0) were created. The positions are illustrated in Fig. 6. The upper and lower limits and calculation steps of the frequency were set to 2900, 1, and 1.613 Hz, respectively, for the acoustic

response calculation.

3. EXPERIMENTAL SYSTEM AND METHOD

3.1 Experimental System

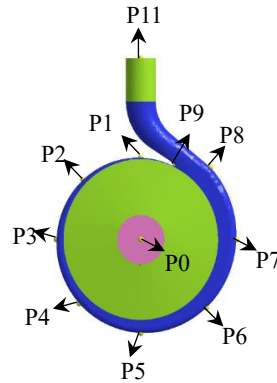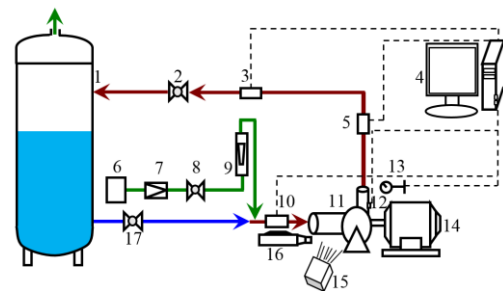To verify the feasibility of the numerical model and

Fig. 6. Location of acoustic field points.

reliability of the simulation results of the flow field, the external characteristics and internal flow of the centrifugal pump were tested. The centrifugal pump experimental system, consisting of the power system, piping system, and data acquisition system, is depicted in Fig. 7. The power system is mainly composed of the motor, rotating shaft, and centrifugal pump. The piping system primarily consists of the water storage tank, metal pipes, and hoses used to connect the various components. The data acquisition system mainly includes the inlet and outlet pressure sensors, turbine flowmeter, rotational speed sensor, and dynamic pressure sensor. The centrifugal pump is driven by the motor, and the impeller rotates at a high speed. The water returns to

1-Water storage tank; 2-Outlet flow rate regulating valve; 3-Turbine flowmeter; 4-Computer; 5-Outlet pressure sensor; 6-Air pump; 7-Pressure reducing valve; 8-Gas control valve; 9-Rotameter; 10-Inlet pressure sensor; 11-Centrifugal pump; 12-Dynamic pressure sensor; 13-Rotational speed sensor; 14-Motor; 15-Cold light source; 16-High-speed camera; 17-Inlet flow rate regulating valve

Fig. 7. Experimental system diagram of the centrifugal pump.

the storage tank through the pipeline, inlet pressure sensor, centrifugal pump, dynamic pressure sensor, outlet pressure sensor, and turbine flowmeter, forming a liquid circulation loop. The gas is produced by the air pump, and its flow rate is controlled by a rotameter. The gas is injected into the suction pipe of the centrifugal pump, delivered to the water storage tank, and finally discharged to the atmosphere.

3.2 Experimental Method

Using the above experimental system, an external characteristic experiment of the centrifugal pump was performed. Owing to the limitations of the experimental conditions, the rotational speed of the centrifugal pump was maintained at 600 rpm by regulating the motor, and the outlet flow rate was adjusted to 7.5, 10, 12.5, 15, and 17.5 m^3/h. When the flow rate was stable, the data from the inlet and outlet pressure sensors, motor torque, and other sensors were collected to obtain the external characteristics of the centrifugal pump.

To further verify the reliability of the numerical simulation results, an Olympus *i*-SPEED 3 high-speed camera was used to photograph the flow in the impeller and volute of the centrifugal pump. The rotational speed was adjusted to 600 rpm, and the liquid and gas flow rates were maintained at 15 m^3/h and 7.5 L/min, respectively. The relative positions of the camera and centrifugal pump when recording the flow in the volute are shown in Fig. 8. The distance between the camera and centrifugal pump is approximately 0.5 m, and the shooting area is near the volute tongue. The shooting frame rate of the high-speed camera was set to 1000 frames/s and the captured image resolution was 1280×1024 pixels.
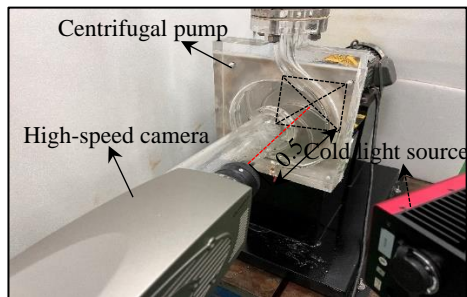

Fig. 8. Arrangement of the centrifugal pump and camera.

4. RESULTS AND DISCUSSION

4.1 Verification of Numerical Calculation Results

4.1.1 Verification of the External Characteristics

To verify the feasibility of the numerical simulation,

the head and efficiency obtained from the simulation were compared with the experimental results, as depicted in Fig. 9. It can be seen that with an increase in the flow rate, the head of the centrifugal pump exhibits a continuous downward trend, and its efficiency first increases and then decreases. The maximum deviations between the head and efficiency obtained from the experiment and numerical simulation are 4.9% and 4.2%, respectively, which are within the deviation range. The numerical simulation results are always higher than the experimental results. This is because in the numerical simulation, the geometric model of the centrifugal pump was simplified. The existence of leakage channels was not considered. Furthermore, the friction loss on the front and rear cover plates, mechanical loss on the bearing and seals, and leakage loss in the wear ring were neglected. Finally, in the setting of the boundary conditions, the inner wall of the centrifugal pump was considered smooth.
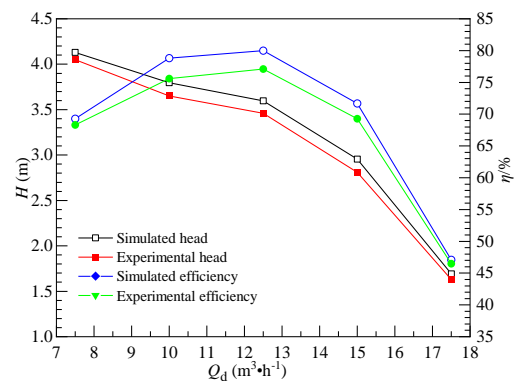

Fig. 9. External characteristic curves of the centrifugal pump.

4.1.2 Verification of the Internal Flow

Figures shows the flow in the impeller and volute obtained by the high-speed camera at different times.

Figure 11 shows the corresponding numerical simulation results. To verify the reliability of the numerical simulation results of the internal flow in the pump during the transition process of gas injection, the numerical simulation results were compared with the internal flow visualisation results.

When $t = 0.54$ s, the gas enters the impeller. At this time, the bubble spacing is relatively large. Moreover, the bubble shape is generally spherical, and there is no aggregation phenomenon. Driven by the rotating impeller, the bubbles move to the outlet of the impeller. When $t = 0.66$ s, the bubbles begin to enter the volute. At this time, the bubble spacing is reduced, the interaction between the bubbles is more evident, and the bubbles appear to aggregate and merge. Under the action of the blades, the large bubbles are cut into smaller bubbles, and the bubbles in the impeller become larger than those in the volute. When $t = 0.91$ s, the

bubbles arrive at the pump outlet, there is no obvious accumulation of bubbles in the volute, and most of them are isolated small bubbles. In the impeller, the pressure pulsation on the pressure side of the blade is relatively low, and the bubbles do not break easily; therefore, a large number of bubbles accumulate on the pressure side. When $t = 2.71$ s, the shape and distribution of the bubbles in the impeller and volute no longer change significantly with time, and the flow in the pump is fully developed at this time.
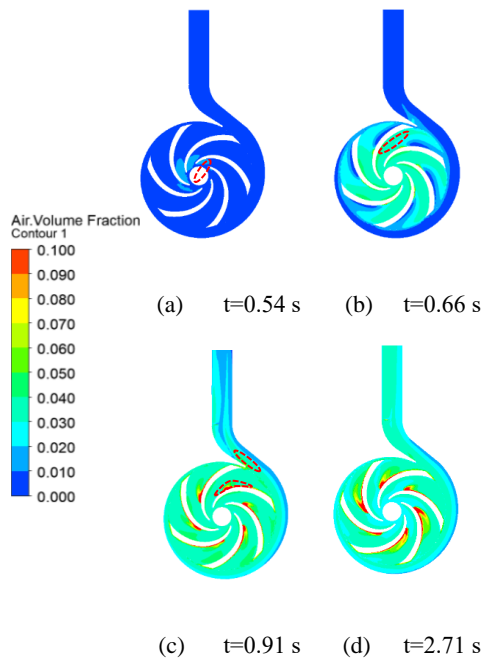

(a)   t=0.54 s   (b)   t=0.66 s

(c)   t=0.91 s   (d)   t=2.71 s

Fig. 10. Visualisation experiment results of the flow in the volute and impeller.

(a) $t = 0.54$ s   (b) $t = 0.66$ s

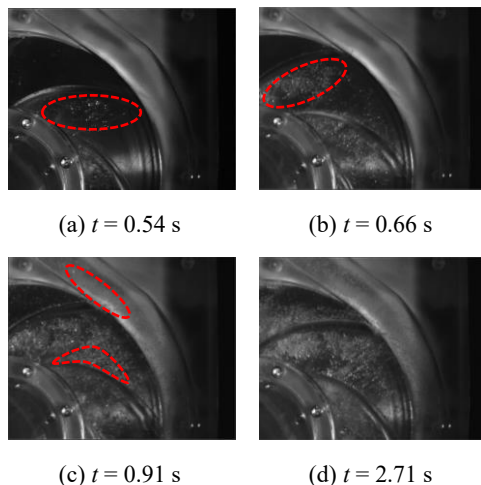(c) $t = 0.91$ s   (d) $t = 2.71$ s

Fig. 11. Numerical simulation results of flow in the pump.

The visual experiment results are consistent with the numerical simulation results. Owing to the influence of the wall roughness and installation error, the bubble movement near the wall in the pump deviates slightly from the numerical simulation result, but the overall bubble distribution and movement law are consistent. Therefore, the numerical simulation is reliable and can be used instead of the experiment.

4.2 Criterion for Judging the End of the Transition Process

4.2.1 Variation of the Pressure at the Pump Outlet with Time

Compared with the unsteady simulation of the single-phase medium, the gas–liquid two-phase numerical simulation is more complex. The accurate determination of the end of the transition process of gas injection is very important for studying the variation law of flow-induced noise in this process. To achieve this goal, the pressure and its time-averaged value at the pump outlet were investigated first.

A numerical simulation was performed under the following operating conditions: rotational speed $n = 2900$ rpm, liquid flow rate $Q_d = 50$ m^3/h, and IGVF = 4%. The pressure fluctuation and time-averaged pressure at the pump outlet are displayed in Fig. 12. At $t = 0$ s, the gas begins to be injected into the pump suction pipe. It can be seen that, when $t < 0.16$ s, compared with that of the stable delivery of the liquid phase medium, the outlet pressure still maintains a quasi-steady state with periodic oscillations, and the time-averaged value of the outlet pressure hardly changes. Therefore, it can be considered that in the early stage of the transition process of gas injection, the gas does not reach the impeller or the amount of gas is very small, and the pressure at the outlet does not change significantly. When 0.16 s $< t < 0.34$ s, the gas gradually reaches the impeller, causing the pressure at the outlet to drop considerably. This further explains why the head of the centrifugal pump conveying the gas–liquid two-phase medium is lower than that of the single-phase medium. When $t > 0.34$ s, the pressure at the outlet recovers a quasi-steady state with periodic oscillations, and the time-averaged value of the pressure almost no longer changes. This can be approximately regarded as the end of the gas injection transition process.

4.2.2 Variation of the GVF at the Pump Outlet with Time

Because the internal flow of a centrifugal pump is extremely complicated, it is not reliable to judge the end of the transition process based only on the pressure at the outlet. Therefore, the outlet GVF (OGVF) was also considered.

The GVF fluctuation curve at the pump outlet is illustrated in Fig. 13. When $t < 0.22$ s, the OGVF is 0, indicating that the gas has not reached the outlet.
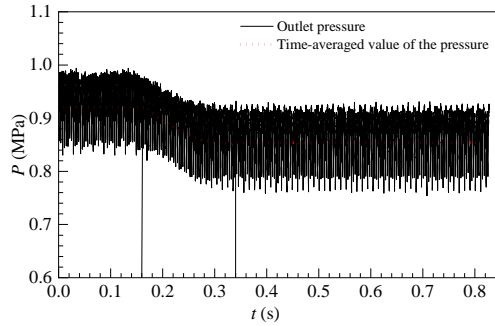
Fig. 12. **Variation of pump outlet pressure with time during the transition process of gas injection.**
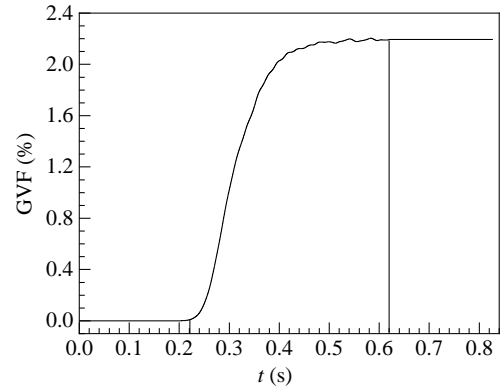

Fig. 13. Variation of pump OGVF with time during the transition process of gas injection.

When 0.22 s < t < 0.62 s, the OGVF increases gradually, indicating that during this period, a large number of bubbles are flowing into the impeller and moving quickly to the pump outlet driven by the rotating blades. When t > 0.62 s, the OGVF tends to be stable. At this time, it can be considered that the transition process of the gas injection is completed.

Based on Figs. 12 and 13, the following can be observed: 1) When t > 0.34 s, the pressure at the outlet enters a periodic fluctuation state, and the time-averaged value of the pressure tends to be stable; however, the OGVF continues to rise, and its distribution in the pump is still not stable. Therefore, it is unreasonable to judge the end of the transition process of the gas injection based only on the periodic fluctuation of the outlet pressure. 2) When t > 0.62 s, the OGVF tends to be stable, and the pressure at the outlet still fluctuates periodically. Therefore, it is more reasonable to consider the stability of the OGVF as the judgement criterion for the end of the gas injection transition process.

4.3 Pressure Pulsation at the Pump Outlet under Different IGVFs

Based on the judgement criterion for the end of the transition process of gas injection and the established end time of the process under various operating conditions, the pressure data at the pump outlet under different IGVFs were Fourier transformed. The effect of the IGVF on the pressure pulsation at the pump outlet was investigated.

When the rotational speed of the impeller is 2900 rpm, we set the impeller rotation at 1° as the time step. That is, the sampling frequency F_S is 17400 Hz, and the maximum frequency that can be used for analysis is 8700 Hz. The upper limit frequency in this study is 10 times the blade frequency.

Therefore, the maximum frequency is higher than the upper limit frequency (2900 Hz), which meets the requirements of the data analysis. After Fourier transformation, the analysis accuracy F_n satisfies Eq. (5). Because the transition process of gas
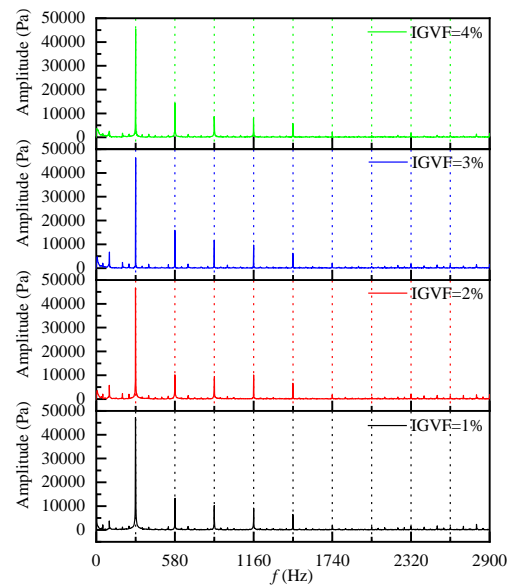

Fig. 14. Pressure fluctuation at the pump outlet during the transition process of gas injection under different IGVFs.

injection exceeds 25 cycles, taking 25 cycles as an example, the analysis accuracy F_n can reach 0.97 Hz, which meets the requirements.

$$F_n = \frac{F_s}{2N} \tag{5}$$

where F_s is the sampling frequency (Hz), F_N is the sampling accuracy (Hz), and N is the number of samples.

The pressure fluctuation at the pump outlet during the transition process of gas injection under different IGVFs is shown in Fig. 14. With an increase in frequency, the amplitude of the pressure pulsation at the outlet exhibits a gradually decreasing trend, indicating that the pressure at the outlet fluctuates significantly in the low-frequency region during the

transition process of gas injection. The extreme value of the pressure pulsation under each operating condition occurs at the BPF and its doubling frequency, and the maximum value appears at the BPF. This indicates that during the transition process of gas injection, the characteristic frequency of the pressure fluctuation at the outlet is the BPF, which further proves that the dynamic and static interferences between the blades and volute are significant. With an increase in IGVF, the amplitude of the pressure pulsation at the outlet decreases slightly. This is because with an increase in the IGVF, the gas is more likely to block the impeller channel and reduce the operating capacity of the pump, which decreases the pressure at the pump outlet and the amplitude of pressure pulsation.
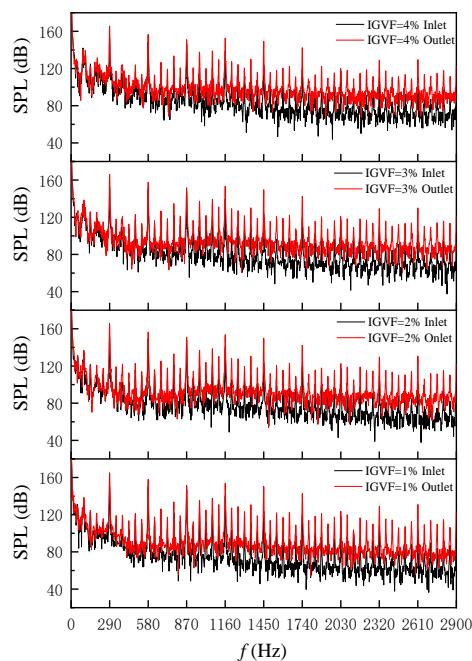
the downstream area. Under all operating conditions, as the frequency increases, the SPL at the outlet gradually decreases. The SPL peaks appear at the BPF, APF, and their doubling frequencies, and the maximum SPL value occurs at the BPF. This indicates that the noise generated by the dynamic and static interferences is higher at low frequencies. The BPF and APF are characteristic discrete frequencies. The broadband noise caused by the turbulence, jet wake, and secondary flow is mostly distributed in the middle- and high-frequency regions.

To determine the influence of the IGVF on the SPL at the outlet, the SPL under different IGVFs was analysed. As displayed in Fig. 16, with an increase in IGVF, the SPL curve generally exhibits an upward trend. This is because, under high IGVF conditions,
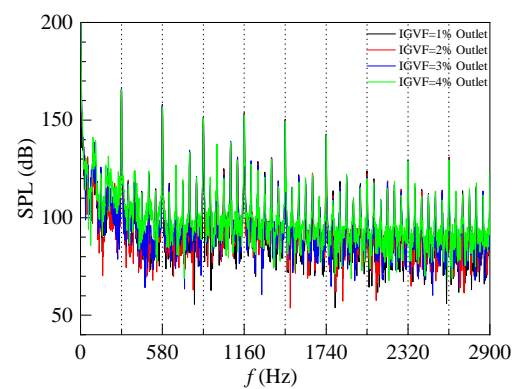

Fig. 16. Frequency-domain SPL curves at the pump outlet under different IGVFs.

Fig. 15. Frequency-domain SPL curves at the pump inlet and outlet under different IGVFs.

4.4 Frequency-domain Sound Field in the Pump during the Transition Process of Gas Injection

4.4.1 Frequency-domain SPL at the Pump Inlet and Outlet

To establish the relationship between the pressure in the flow field and the SPL in the sound field, based on the above analysis of the flow field in the pump during the transition process of gas injection, acoustic numerical simulations at IGVFs of 1%, 2%, 3%, and 4% were carried out. The frequency-domain SPL curves at the pump inlet and outlet under different IGVFs are depicted in Fig. 15. The SPL at the pump outlet is higher than that at the inlet under all operating conditions, indicating that the flow-induced noise in the pump is mostly concentrated in
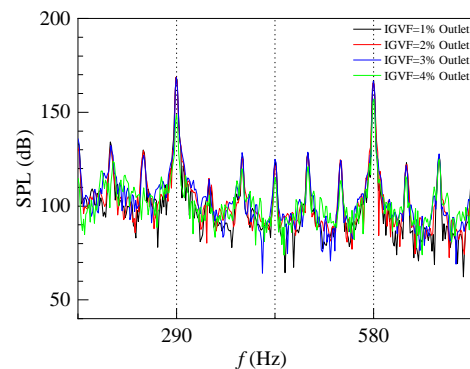

Fig. 17. Enlarged portion of the SPL curve at the outlet.

the internal flow of the pump is more complicated, and the turbulence intensity is considerably increased, resulting in a significant increase in the broadband noise. It can be concluded from the enlarged portion of the SPL curve in Fig. 17 that the BPF and APF are both discrete characteristic frequencies. At these characteristic frequencies, the SPL exhibits a downward trend as the IGVF increases. This is because at these frequencies, an increase in the IGVF causes the amplitude of the

pressure pulsation at the pump outlet to decrease, resulting in a downward trend of the SPL.

4.4.2 SPL Distribution in the Pump

From the above analysis, the APF and BPF are the characteristic discrete frequencies in the transition process of gas injection. Based on this, the SPL distribution characteristics of the pump under different IGVFs at the APF and BPF were thoroughly evaluated. The SPL distributions in the pump under different IGVFs at the APF are illustrated in Fig. 18. Under all operating conditions, the SPL at the front cover of the impeller is the smallest and that at the volute tongue is the highest. The SPL in the volute exhibits a gradually increasing trend in the flow direction. This phenomenon can be
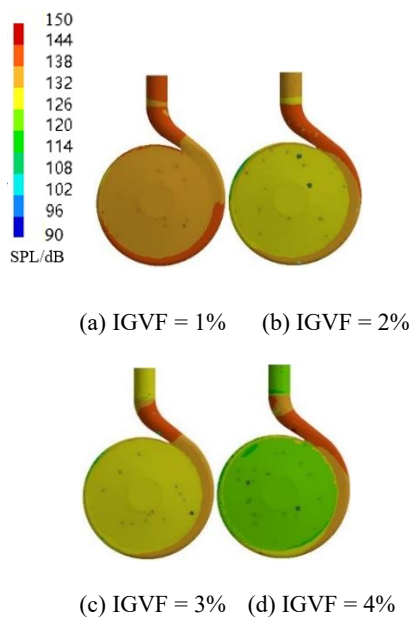

(a) IGVF = 1%   (b) IGVF = 2%

(c) IGVF = 3%   (d) IGVF = 4%

Fig. 18. **Distributions of the SPL in the pump under different IGVFs at the APF**.

explained as follows: The centrifugal pump converts mechanical energy into fluid pressure energy; thus, the downstream fluid has a higher pressure energy, and the impact on the volute wall is more intense, which strengthens the pressure pulsation and gradually increases the SPL on the volute wall. At the APF, the IGVF has a significant influence on the SPL distribution in the pump. With an increase in the IGVF, the SPL at the pump outlet and front cover plate shows an obvious downward trend.

The SPL distributions in the pump under different IGVFs at the BPF are depicted in Fig. 19. Under different IGVFs, the SPL at the front cover plate of the impeller is low, whereas that at the volute tongue is the highest. However, along the flow direction, the SPL in the volute no longer exhibits an evident law. This is because at the BPF, the blades frequently cut bubbles during rotation. This increases the flow
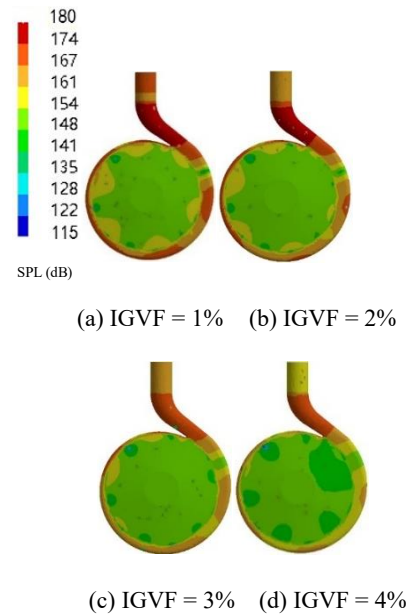

(a) IGVF = 1%   (b) IGVF = 2%

(c) IGVF = 3%   (d) IGVF = 4%

Fig. 19. Distributions of the SPL in the pump under different IGVFs at the BPF.

complexity and makes the pressure pulsation in the pump different, which results in a local low sound pressure zone. With an increase in IGVF, the six relatively uniform wave peaks distributed on the front cover plate of the impeller no longer appear but gradually spread until the front cover plate is completely covered. Moreover, the SPL at the BPF in the pump exhibits a downward trend. This is because the injection of gas weakens the disturbance effect of the blades, so that the pressure pulsation in the pump at this frequency decreases as a whole, and the SPL of the internal field at the BPF decreases gradually with an increase in the IGVF.

4.5 Time-domain Sound Field in the Pump during the Transition Process of Gas Injection

4.5.1 Variation Law of the Amplitude and SPL with Time at the BPF

Based on the analysis of the frequency-domain sound field in the pump, the time-domain sound field during the transition process of gas injection was evaluated. The variation in the amplitude of the pressure pulsation with time at each monitoring point is shown in Fig. 20. whereas the variation in the SPL with time is depicted in Fig. 21. From Figs. 20 and 21, the following phenomena can be observed, and the corresponding conclusions can be drawn. 1). In the early stage of the transition process ($t < 0.16$ s), the pressure in the pump maintains a quasi-steady state with periodic oscillations, the pressure pulsation is constant, and the SPL remains unchanged. 2) In the middle stage of the transition process (0.16 s $< t <$ 0.34 s), the pressure inside the

pump drops with the continuous injection of gas. The pressure fluctuation intensifies and exhibits a trend of first decreasing and then increasing with time. The
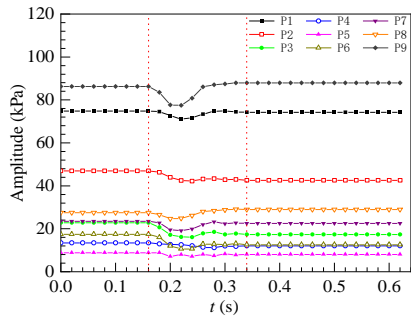

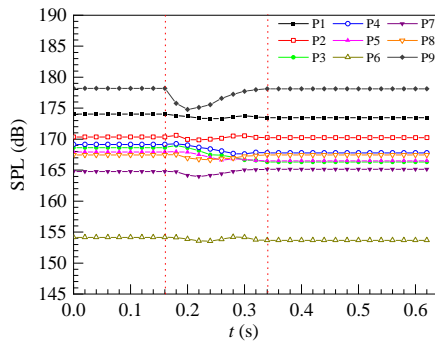**Fig. 20. Time-domain pressure fluctuation curve of each monitoring point at the BPF**

Fig. 21. Time-domain SPL curve of each monitoring point at the BPF.

SPL variation law is consistent with the pressure pulsation. 3) In the late stage of the transition process ($t > 0.34$ s), the pressure in the pump returns to a quasi-steady state with periodic oscillations. The pressure pulsation in the pump maintains a stable state, and the SPL at all locations tends to be stable. 4) The change in pressure pulsation is the direct factor leading to the change in SPL, and the variation law between the two is consistent. The SPL after stabilisation is slightly lower than the initial SPL. This indicates that gas injection can weaken the disturbance effect of the blade to a certain extent. Thus, the pressure pulsation and ultimately the SPL are reduced.

4.5.2 Time-Domain SPL Distribution of the Sound Field at the BPF

Based on the investigation of the time-domain SPL of each monitoring point at the BPF, the transition process of gas injection is divided into three stages: early, middle, and late. The distributions of the SPL in the pump at different times in each stage are illustrated in Fig. 22. In the early stage of the transition process ($t < 0.16$ s), the pressure in the pump fluctuates periodically, the pressure pulsation

under the BPF is constant, and the SPL in the pump remains unchanged. However, with the continuous injection of gas, the middle stage of the transition process occurs (0.16 s $< t < 0.34$ s). During this stage, the pressure in the pump decreases, and the amplitude of the pressure pulsation first decreases and then increases slightly, resulting in a noticeable decrease and then a small increase in the SPL. In the late stage of the transition process ($t > 0.34$ s), the pressure in the pump returns to a state of stable periodic fluctuation, and the amplitude of the pressure pulsation at the BPF becomes constant. Because the gas weakens the disturbance of the blade, the SPL in the pump in the final stable gas–liquid two-phase flow state is lower than that in the initial single-phase state.

The following conclusions can be drawn based on the analysis of the results shown in Fig. (22. 1) During the transition process of gas injection, the
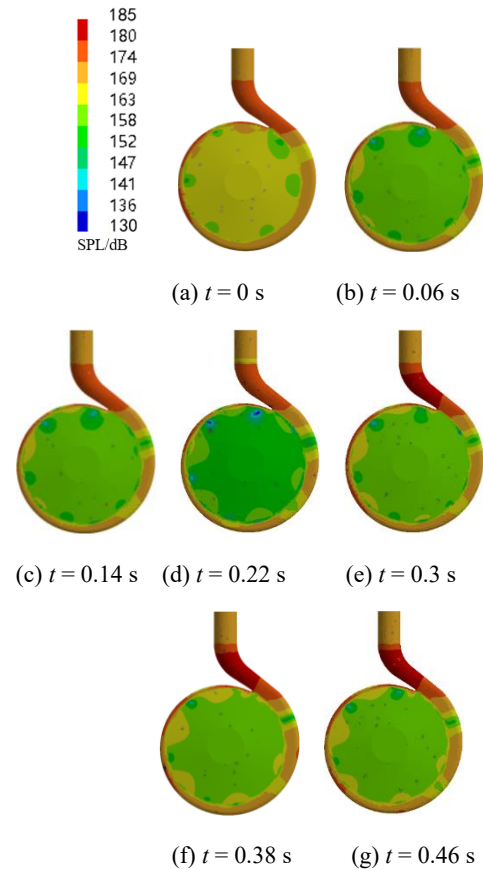

(a) $t = 0$ s   (b) $t = 0.06$ s

(c) $t = 0.14$ s   (d) $t = 0.22$ s   (e) $t = 0.3$ s

(f) $t = 0.38$ s   (g) $t = 0.46$ s

Fig. 22. Distribution of the sound field at the BPF in the pump at different times.

SPL in the pump is stable at the beginning, decreases and increases, and finally returns to a stable state. With the continuous injection of gas, both the disturbance effect of the blade and SPL in the pump decrease significantly. 2) The variation in pressure pulsation is consistent with that of the SPL. The pressure pulsation is directly induced by the change in the SPL. The gas injection can effectively reduce

the pressure pulsation at the BPF such that the SPL in the pump at the BPF is reduced.

5. CONCLUSION

In this study, the impact of transient gas injection on the flow-induced noise in a centrifugal pump was investigated. The main conclusions are as follows:

1) It is more reasonable to consider the OGVF as the judgement criterion for the end of the transition process of gas injection than the pump outlet pressure. With an increase in the IGVF, the pressure pulsation at the pump outlet decreases.

2) Both the BPF and APF are characteristic discrete frequencies of the flow-induced noise in the pump during the gas injection process. With an increase in the IGVF, the broadband noise caused by the internal turbulence and secondary flow increases significantly, and the SPL in the pump at the APF and BPF exhibits a downward trend. This indicates that the injection of gas can effectively weaken the disturbance effect of the blade, thereby reducing the SPL.

3) The transition process of gas injection and the variation laws of the pressure pulsation and SPL are consistent, indicating that the pressure fluctuation is the direct effect of the change in the SPL.

REFERENCES

Crighton, D. G. (1972). Radiation from vortex filament motion near a half plane. *Journal of Fluid Mechanics* 51(2), 357-362.

Curle, N. (1955). The influence of solid boundaries upon aerodynamic sound. *Proceedings of the Royal Society of London. Series A. Mathematical and Physical Sciences* 231(1187), 505-514.

Dong, L., C. Dai, H. B. Lin and Y. P. Chen (2018). Noise comparison of centrifugal pump operating in pump and turbine mode. *Journal of Central South University* 25(11), 2733-2753.

Gao, M., P. X. Dong, S. H. Lei and A. Turan (2017). Computational study of the noise radiation in a centrifugal pump when flow rate changes. *Energies* 10(2), 221.

Goldstein, J. L. (1973). An optimum processor theory for the central formation of the pitch of complex tones. *Journal of the Acoustical Society of America* 54(6), 1496-1516.

Guo, C., M. Gao, J. Y. Wang, Y. T. Shi and S. Y. He (2019). The effect of blade outlet angle on the acoustic field distribution characteristics of a centrifugal pump based on Powell vortex sound theory. *Applied Acoustics* 155, 297-308.

He, A. X. and C. L. Shao (2021). Study on the induced noise of gas-liquid two-phase flow in a centrifugal pump. *Applied Acoustics* 176, 107892.

Jaiswal, A. J., M. H. Siddique, A. R. Paul and A. Samad (2022). Surrogate-based design optimization of a centrifugal pump impeller. *Engineering Optimization* 54(8), 1395-1412.

Jaiswal, A. K., A. U. Rehman, A. R. Paul and Jain, A. (2019). Detection of cavitation through acoustic generation in centrifugal pump impeller. *Journal of Applied Fluid Mechanics* 12(4), 1103-1113.

Jiang, Y. Y., S. Yoshimura, R. Imai, T. Katsura and C. Kato (2007). Quantitative evaluation of flow-induced structural vibration and noise in turbo machinery by full-scale weakly coupled simulation. *Journal of Fluids and Structures* 23(4), 531-544.

Kalyan, D. K., A. U. Rehman, A. R. Paul and A. Jain (2013). Computational flow analysis through a double-suction impeller of A centrifugal pump. In *Proceedings of the Fortieth National Conference on Fluid Mechanics and Fluid Power*, Himachal Pradesh, India.

Langthjem, M. A. and N. Olhoff (2004). A numerical study of flow-induced noise in a two-dimensional centrifugal pump. Part II. Hydroacoustics. *Journal of Fluids and Structures* 19(3), 369-386.

Lighthill, M. J. (1953). On sound generated aerodynamically I. General theory. *Proceedings of the Royal Society of London. Series A. Mathematical and Physical Sciences* 211(1107), 564-587.

Lighthill, M. J. (1954). On sound generated aerodynamically II. Turbulence as a source of sound. *Proceedings of the Royal Society of London. Series A. Mathematical and Physical Sciences* 222(1148), 1-32.

Liu, H. L., H. W. Dai, J. Ding, M. G. Tan, Y. Wang and H. Q. Huang (2016). Numerical and experimental studies of hydraulic noise induced by surface dipole sources in a centrifugal pump. *Journal of Hydrodynamics* 28(1), 43-51.

Luan, H. X., Q. G. Chen, L. Y. Weng, Z. Y Luan and J. Li (2016). Numerical computation of the flow noise for the centrifugal pump with considering the impeller outlet width. *Journal of Vibroengineering* 18(4), 2601-2612.

Mousmoulis, G., N. Karlsen-Davies, G. Aggidis, L. Anagnostopoulos and D. Papantonis (2019). Experimental analysis of cavitation in a centrifugal pump using acoustic emission, vibration measurements and flow visualization. *European Journal of Mechanics B-Fluids* 75, 300-311.

Rehman, A. U., A. R. Paul and A. Jain (2017). Effect of impeller volute interaction on performance

of the centrifugal pump: a CFD approach. *Indian conference on applied mechanics* 52(11), 241-242.

Rehman, A. U., A. R. Paul and A. Jain (2019). Performance analysis and cavitation prediction of centrifugal pump using various working fluids. *Recent Patents on Mechanical Engineering* 12, 227-239.

Rehman, A. U., S. Shinde, V. K. Singh, A. R. Paul, A. Jain and R. Mishra (2013). CFD based condition monitoring of centrifugal pump. In *COMADEM 2013*, Helsinki.

Rehman, A. U., S. Shinde, A. R. Paul and A. Jain (2015a). Effects of discharge on the performance of an industrial centrifugal pump. In *Proceedings of 2015 International Conference on Computing Techniques and Mechanical Engineering*, Phuket.

Rehman, A. U., S. Srivastava, A. Jaina, A. R. Paul and R. Mishra (2015b). Effect of blade trailing edge angle on the performance of a centrifugal pump impeller. In *28th International Congress of Condition Monitoring and Diagnostic Engineering.*

Rui, X. P. and Y. Zhao (2016). Numerical simulation and experimental research of flow-induced noise for centrifugal pumps. *Journal of Vibroengineering* 18(1), 622-636.

Shao, C. L., G. C. Zhong and J. F. Zhou (2021a). Study on gas-liquid two-phase flow in the suction chamber of a centrifugal pump and its dimensionless characteristics. *Nuclear Engineering and Design* 380, 111298.

Shao, C. L., N. Bao, S. Wang and J. F. Zhou (2021b). Study on the prediction method and the flow characteristics of gas-liquid two-phase flow patterns in the suction chamber. *International Journal of Numerical Methods for Heat & Fluid Flow* 32(8), 2700-2718.

Si, Q. R., C. H. Shen, X. K. He, H. Li, K. Huang and J. P. Yuan (2020). Numerical and experimental study on the flow-induced noise characteristics of high-speed centrifugal pumps. *Sn Applied Sciences* 10(9), 3105.

Si, Q. R., S. Q. Yuan, J. P. Yuan and Y. Liang (2013). Investigation on flow-induced noise due to backflow in low specific speed centrifugal pumps. *Advances in Mechanical Engineering* 5, 109048.

Wang, L., H. L. Liu, K.Wang, L. Zhou, X. P. Jiang and Y. Li (2019). Numerical simulation of the sound field of a five-stage centrifugal pump with different turbulence models. *Water-Sui* 11(9), 1777.

Wang, Y. Q. and Z. W. Ding (2020). Influence of blade number on flow-induced noise of centrifugal pump based on CFD/CA. *Vacuum* 172, 109058.

Wang, Y., B. F. Song, W. P. Song and J. Ren (2017). Numerical computation for the impact of flow rate and rotational speed on the flow-induced noise of the centrifugal pump. *Journal of Vibroengineering* 19(8), 6455-6470.